NANO LETTERS

pubs.acs.org/NanoLett

Letter

Larger-Than-Unity External Optical Field Confinement Enabled by Metamaterial-Assisted Comb Waveguide for Ultrasensitive Long-Wave Infrared Gas Spectroscopy

Weixin Liu,[§] Yiming Ma,[§] Xinmiao Liu, Jingkai Zhou, Cheng Xu, Bowei Dong, and Chengkuo Lee*

Cite This: *Nano Lett.* 2022, 22, 6112–6120

Read Online

ACCESS | Metrics & More | Article Recommendations | Supporting Information

ABSTRACT: Nanophotonic waveguides that implement long optical pathlengths on chips are promising to enable chip-scale gas sensors. Nevertheless, current absorption-based waveguide sensors suffer from weak interactions with analytes, limiting their adoptions in most demanding applications such as exhaled breath analysis and trace-gas monitoring. Here, we propose an all-dielectric metamaterial-assisted comb (ADMAC) waveguide to greatly boost the sensing capability. By leveraging large longitudinal electric field discontinuity at periodic high-index-contrast interfaces in the subwavelength grating metamaterial and its unique features in refractive index engineering, the ADMAC waveguide features strong field delocalization into the air, pushing the external optical field confinement factor up to 113% with low propagation loss. Our sensor operates in the important but underdeveloped long-wave infrared spectral region, where absorption fingerprints of plentiful chemical bonds are located. Acetone absorption spectroscopy is demonstrated using our sensor around 7.33 μm, showing a detection limit of 2.5 ppm with a waveguide length of only 10 mm.

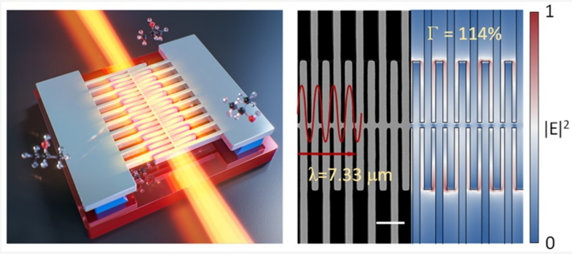

KEYWORDS: *absorption spectroscopy, waveguide sensors, long-wave infrared, all-dielectric metamaterial, silicon photonics*

Optical sensors have experienced rapid advancement over the past decade in the ever-growing field of gas sensing, with applications ranging from environmental monitoring to medical diagnostics.[1−9] Among various optical sensing technologies, infrared tunable diode laser absorption spectroscopy (IR-TDLAS) is the one that targets the "fingerprints" derived from rovibrational transitions of molecules, enabling label-free analysis with inherent selectivity, which is promising for multiplexed sensing in complex environments.[10,11] In particular, nanophotonic waveguides that implement long optical pathlengths on chips enable the development of compact, fieldable, and cost-effective on-chip IR-TDLAS sensors for large-scale sensor deployment.[12−14]

Nevertheless, most of the current waveguides that probe analytes via the evanescent fields still suffer from a weak light−matter interaction limited to a fraction of that for a free-space beam, hindering their applications in sensitivity-critical scenarios.[15−19] The external optical field confinement factor Γ gives a measure of light−matter interaction strength in waveguide that follows the Beer−Lambert law (i.e., the absorbance $A = \varepsilon c \Gamma l = \log(I_0/I)$, where ε is the molar absorption coefficient, c is the analyte concentration, and l is the physical waveguide length).[20] To enhance the Γ, several alternatives to conventional strip waveguides have been proposed. For example, by suspending a thin Si strip waveguide with supporting pillars, Ottonello-Briano et al. achieved a Γ of 44% at 4.24 μm.[21] It is worth noting that Γ accounts for both field distribution and waveguide dispersion, which makes a Γ larger than unity possible. Recently, by leveraging strong transverse magnetic (TM) field delocalization with a moderate dispersion, Vlk et al. demonstrated a Γ of 107% at 2.566 μm in a suspended tantalum pentoxide rib waveguide.[22] However, the vertically wide distributed mode requires a large gap separation of 20 μm between the waveguide and the substrate, which not only results in a mechanically fragile high-aspect-ratio membrane structure but also is hard to implement on conventional waveguide platforms due to insulator thickness constraints. An even higher Γ enabled by strong dispersion in slow light photonic-crystal waveguides have been claimed.[23,24] Nevertheless, their performance is limited by high propagation loss and is susceptible to fabrication errors.

All-dielectric metamaterials, offering a dissipationless alternative to current metallic metamaterials to manipulate light at the nanoscale, have recently emerged as a flexible toolkit for various metadevices with significantly enhanced effi-

Received: March 24, 2022
Revised: June 23, 2022
Published: June 27, 2022

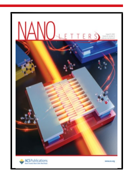

https://doi.org/10.1021/acs.nanolett.2c01198
Nano Lett. 2022, 22, 6112–6120

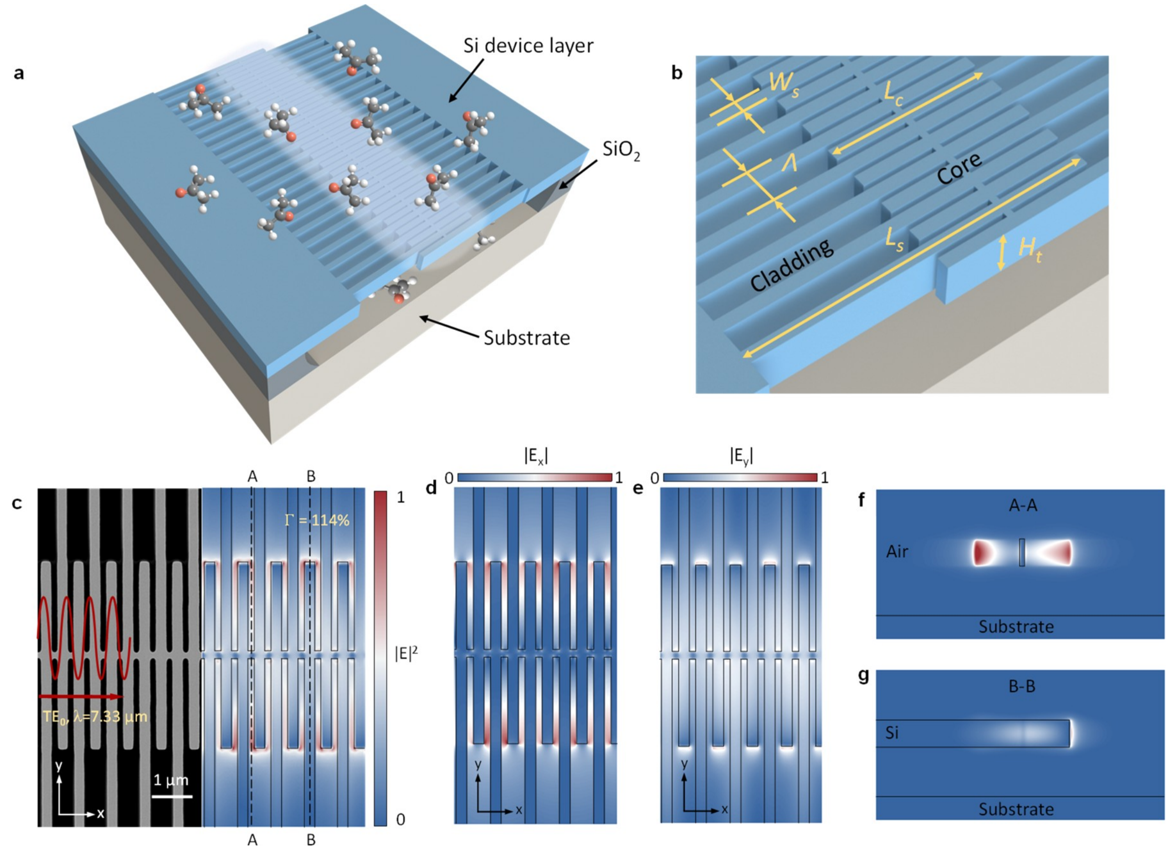

Figure 1. Waveguide structure and the simulated optical field distribution. (a) Schematic diagram of the LWIR ADMAC waveguide with a 1.5 μm thick device layer and a 3 μm thick BOX layer. The waveguide is patterned in the Si device layer with the underneath SiO_2 locally wet etched to suspend the waveguide. (b) Geometric parameters of the ADMAC waveguide include the grating thickness H_t, period Λ, length L_s, width W_s, and overlap width L_c. (c) Top-view SEM image of the ADMAC waveguide with a period of 0.8 μm and duty cycle of 0.3 and $|E|^2$ distribution of the fundamental TE mode at the wavelength of 7.33 μm. The corresponding (d) $|E_x|$ and (e) $|E_y|$ distributions. The corresponding $|E|^2$ distributions at (f) cross sections of the air gap and (g) the Si beam as depicted in (c).

ciency.[25−30] In particular, non-resonant metamaterials with structure sizes considerably below the operating wavelength have moved into the focus of integrated photonics with its unique properties to shape the optical field distribution and engineer the local refractive index (RI). To date, on-chip deployments of non-resonant all-dielectric metamaterials have enabled the realizations of high-performance and ultracompact building blocks, such as metalenses,[31,32] beam splitters,[33,34] and extreme-skin-depth waveguides,[35,36] for dense photonic integration. On top of these realizations, the properties of all-dielectric metamaterials in optical field shaping and RI engineering will also provide great opportunities to realize easily fabricated and low-loss on-chip IR-TDLAS systems with superior light−matter interactions.[37]

Here, we propose an ultrasensitive all-dielectric metamaterial-assisted comb (ADMAC) waveguide sensor featuring a larger-than-unity external confinement factor as well as a low propagation loss. The waveguide is fabricated from the most mature silicon-on-insulator (SOI) platform with CMOS-compatible techniques. The extraordinary optical field confinement is enabled by large longitudinal electric field discontinuity at periodic high-index-contrast Si/air interfaces in the subwavelength grating (SWG) metamaterial, together with its unique features in RI engineering. Our ADMAC waveguide is operated in the long-wave infrared (LWIR, 6−14 μm) spectral region that covers plentiful molecular absorption fingerprints, which is nevertheless underdeveloped in comparison to the short- and mid-wave infrared (SWIR, 1−3 μm; MWIR, 3−6 μm) due to severe absorption from bottom cladding materials in most of the currently well-established waveguide platforms.[38−43] To enable the SOI for LWIR operation, the absorptive buried oxide (BOX) beneath the waveguide is locally removed. Meanwhile, thanks to the deep-subwavelength operation and the vertically well confined mode distribution, the ADMAC waveguide possesses a low propagation loss over a wide wavelength range and is not susceptible to fabrication errors. By optimizing the period and duty cycle of the ADMAC waveguide, we achieve an Γ of 113% with a low propagation loss of 4.7 dB/cm at 7.33 μm. Spectroscopic sensing of acetone vapor is performed on a 10 mm long waveguide, showing a detection limit of 10 ppm with a fast dynamic response, which can be further decreased to 2.5 ppm with a moderate averaging time. The results indicate the promising potential of our ADMAC waveguide for widespread real-time on-site sensing applications.

For the waveguide design, two sets of SWG metamaterial beams with a period Λ form the interdigitated comb structure, in which light is guided through the overlap region (Figure 1a). A 150 nm wide Si wire is added in the middle of the comb structure to avoid the adhesion between adjacent free-standing beams. The grating period is chosen to satisfy the subwavelength condition, that is, $\Lambda \ll \lambda/(2n_{\mathrm{eff}})$, where n_{eff} is the waveguide mode effective index.[44,45] At the overlap region, the period is reduced to $\Lambda/2$, making our waveguide work in

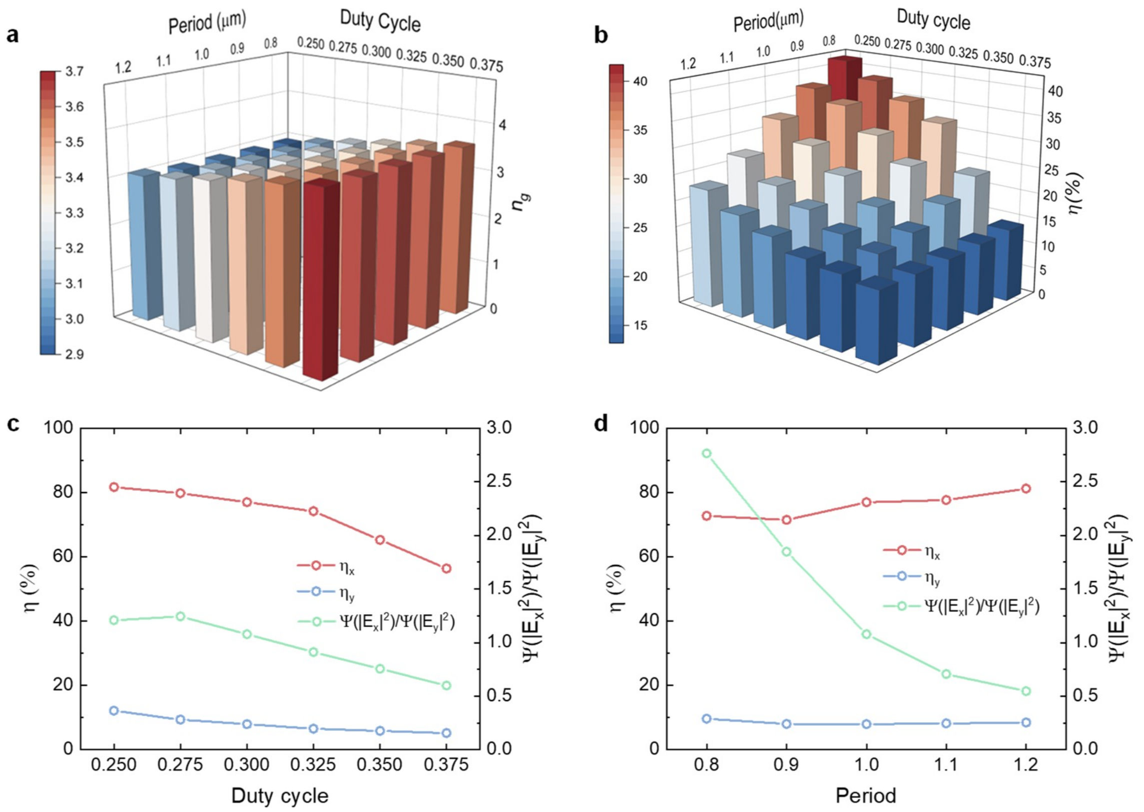

Figure 2. Group index and η of ADMAC waveguides. (a) Simulated group index and (b) η with respect to the period and duty cycle of ADMAC waveguides. To eliminate the lateral leakage loss and provide adequate mechanical support, the grating length L_s and the overlap width L_c are kept at 10 and 4.5 μm, respectively. The period range is chosen to meet the subwavelength working condition (upper limit) as well as the fabrication constraint (lower limit). The duty cycle range is chosen to meet the fabrication constraint (upper limit) as well as to reduce substrate/lateral leakages (lower limit). (c) η_x and η_y components, as well as $\psi(|E_x|^2)/\psi(|E_y|^2)$ with different duty cycles, while the period is fixed as 1.0 μm. (d) η_x and η_y components, as well as $\psi(|E_x|^2)/\psi(|E_y|^2)$ with different periods, while the duty cycle is fixed as 0.3.

the deep-subwavelength regime, where reflection and diffraction effects are significantly suppressed. We define the duty cycle of ADMAC waveguide as W_s/Λ, where W_s is the width of the Si beam (Figure 1b). The core and the lateral cladding of the ADMAC waveguide behave like homogeneous materials with different equivalent RIs, depending on both the period Λ and the duty cycle. This gives our ADMAC waveguide the flexibility to engineer the local RI as well as the mode profile (see Note 1 in the Supporting Information). In the comb configuration, the optical field is greatly enhanced and confined in air gaps between Si beams (Figure 1c). This is mainly attributed to the large discontinuity of longitudinal electric field E_x at high-index-contrast interfaces between Si and air along the propagation direction, with much higher amplitude in the low-index air, to satisfy the continuity of the normal component of electric flux density D governed by Maxwell's equations (see Figure 1d and Note 2 in the Supporting Information). Particularly, E_x that strongly confined in the air gap is the propagation wave instead of the evanescent wave, which results in the field remaining high all across the air gap without an exponential decay. Although the transverse electric field E_y also shows discontinuity along the lateral direction (Figure 1e), its continuity along the propagation direction still localizes a large portion of the electric field in the Si beam and, consequently, E_y contributes a weaker enhancement of Γ in comparison to E_x. Figure 1f,g presents optical fields at cross sections of the air gap and the Si beam in Figure 1c, respectively. It is noteworthy that optical fields are laterally strongly delocalized but vertically well confined, leading to a negligible light penetration into the substrate with a BOX layer of only 3 μm thick. This is enabled by the relatively high RI contrast in the vertical direction between the core and top/bottom air claddings, in comparison to that in the lateral direction (see Note 1 in the Supporting Information). Moreover, the presence of the central wire has a negligible disturbance of the optical field due to the strong field delocalization in the lateral direction.

The external confinement factor Γ, which depends on both field distribution and group index n_g, is quantified via perturbation theory[20]

$$\Gamma = \frac{d_{n_{\mathrm{eff}}}}{d_{n_{\mathrm{clad}}}} = \frac{n_g}{n_{\mathrm{clad}}}\eta = \frac{n_g}{n_{\mathrm{clad}}} \frac{\iiint_{\mathrm{clad}} \varepsilon\,|\mathbf{E}|^2\,\mathrm{d}x\,\mathrm{d}y\,\mathrm{d}z}{\iiint_{-\infty}^{\infty} \varepsilon\,|\mathbf{E}|^2\,\mathrm{d}x\,\mathrm{d}y\,\mathrm{d}z} \quad (1)$$

where n_{clad} is the RI of air cladding and is consistently 1, $\varepsilon(x, y, z)$ is the spatial permittivity, $\mathbf{E}(x, y, z)$ is the spatial electric field, and η is the fraction of electric field energy density in the air that does not account for the waveguide dispersion. Our ADMAC waveguide offers great tunability of attainable electric field distributions and the consequent η by engineering its period and duty cycle, while its group index shows less variation due to the deep-subwavelength working status (Figure 2a,b) (see Note 3 in the Supporting Information for simulation methods). Within the studied range, η monotonically increases with decreasing period and duty cycle. To further understand this dependence of η on period and duty

https://doi.org/10.1021/acs.nanolett.2c01198
Nano Lett. 2022, 22, 6112−6120

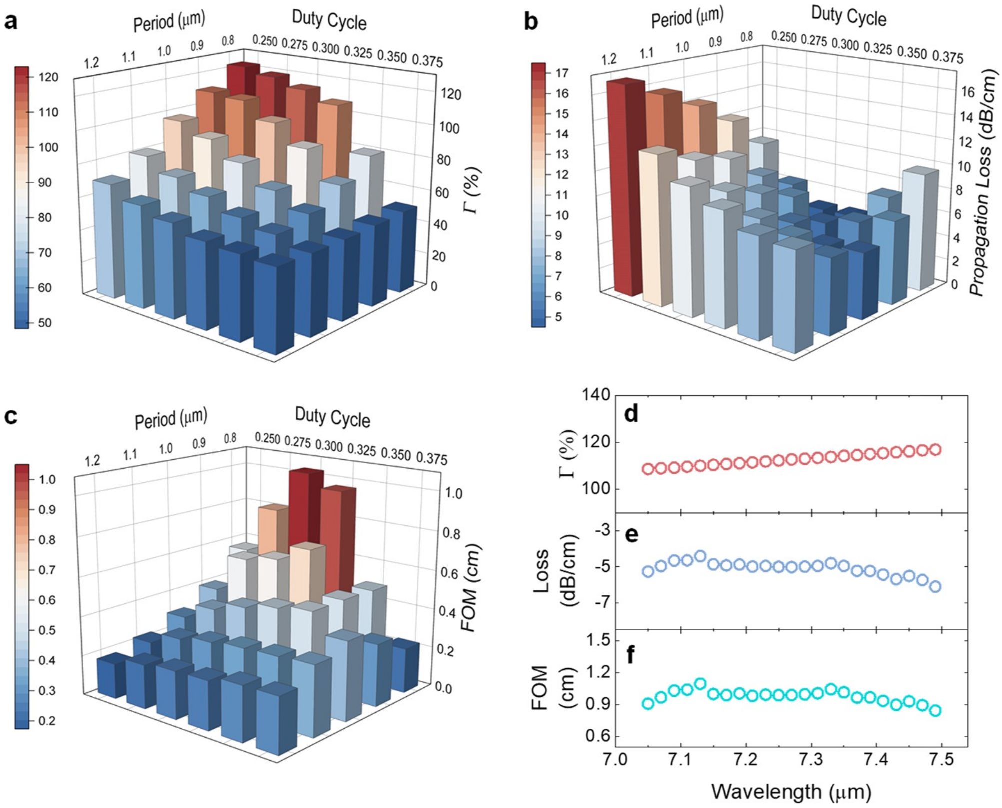

Figure 3. Optimization and the spectral response of ADMAC waveguides. (a) Simulated Γ, (b) measured propagation loss, and (c) calculated FOM with respect to the period and duty cycle of ADMAC waveguides. For the propagation loss matrix, each data point is extracted from cutback measurements of waveguides with different lengths to eliminate deviation induced by fabrication imperfection. (d) Wavelength-dependent Γ, (e) propagation loss, and (f) FOM of the ADMAC waveguide with a period of 0.8 μm and a duty cycle of 0.3.

cycle, we study the contributions from η_x and η_y components separately, as well as the ratio $\psi(|E_x|^2)/\psi(|E_y|^2)$, as depicted in Figure 2c,d. η_x (η_y) is the fraction of E_x (E_y) energy density in the air, $\psi(|E_x|^2)$ ($\psi(|E_y|^2)$) is the spatial integration of $|E_x|^2$ ($|E_y|^2$), and $\psi(|E_x|^2)/\psi(|E_y|^2)$ gives a measure of the relative proportion of these two electric field components. For a larger duty cycle, both η_x and η_y drop due to the larger proportions of Si along the propagating path and therefore less field delocalization into the air (Figure 2c). Figure 2d shows that η_x and η_y undergo less variation with the comb period. Nevertheless, the ratio $\psi(|E_x|^2)/\psi(|E_y|^2)$ obviously decreases with increasing period due to the decreasing n_{cont} in the lateral direction (see Note 1 in the Supporting Information).[46] As the major field delocalization is enabled by E_x distribution, the boosted external field confinement by the E_x component is greatly compensated by the E_y component in the ADMAC waveguide with a larger period, thus leading to a smaller overall η. The product of the group index and η gives the Γ matrix as presented in Figure 3a, which shows a trend similar to that of the η matrix. Consequently, with a period of 0.8 μm and a duty cycle of 0.3, the strong field delocalization and moderate group index bring the Γ above unity to 114% (Figure 1c).

As a key factor of IR-TDLAS sensors to enable sensitivity-critical applications, the limit of detection (LoD) depends on not only the light−matter interaction strength given by Γ but also the interaction length limited by propagation loss. Here we use the figure of merit

$$\mathrm{FOM} = \frac{\Gamma}{\alpha} \tag{2}$$

to quantify the sensing performance of IR-TDLAS sensors,[21,47] where α is the waveguide attenuation coefficient, including material, scattering, and substrate losses (see Note 4 in the Supporting Information for details). To acquire the FOM of ADMAC waveguides with respect to the period and duty cycle, waveguides with different parameters were fabricated by single-step electron-beam lithography and characterized with a fiber-coupled spectroscopy setup (see Note 5 in the Supporting Information). The details of fabrication procedures can be found in Note 6 in the Supporting Information. The propagation loss matrix of ADMAC waveguides at 7.33 μm for transverse electric (TE) polarization is depicted in Figure 3b. A minimum propagation loss of 4.8 dB/cm was recorded with a comb period of 0.8 μm and a duty cycle of 0.3, which is comparable to the values of previously reported LWIR waveguides (see Note 7 in the Supporting Information).[48−51] For waveguides with a large period, the extra loss is mainly attributed to the diffraction from the lateral cladding that is getting closer to the Bragg regime. For waveguides with a small duty cycle, the loss is raised by the substrate and lateral leakage due to the reduced n_{eff} and therefore expanded mode field (see Note 1 in the Supporting Information). For waveguides with both a large duty cycle and a small period, the loss is also increased. This is likely due to the increased scattering loss at rougher sidewalls as the size approaches the fabrication limit. The FOM of ADMAC waveguides then can be calculated by eq 2, and the results are shown in Figure 3c. A maximum FOM of 1.03 cm is achieved in the optimized waveguide with a period of 0.8 μm and a duty cycle of 0.3. To further study the spectral properties of this optimized waveguide, we simulated

https://doi.org/10.1021/acs.nanolett.2c01198
Nano Lett. 2022, 22, 6112−6120

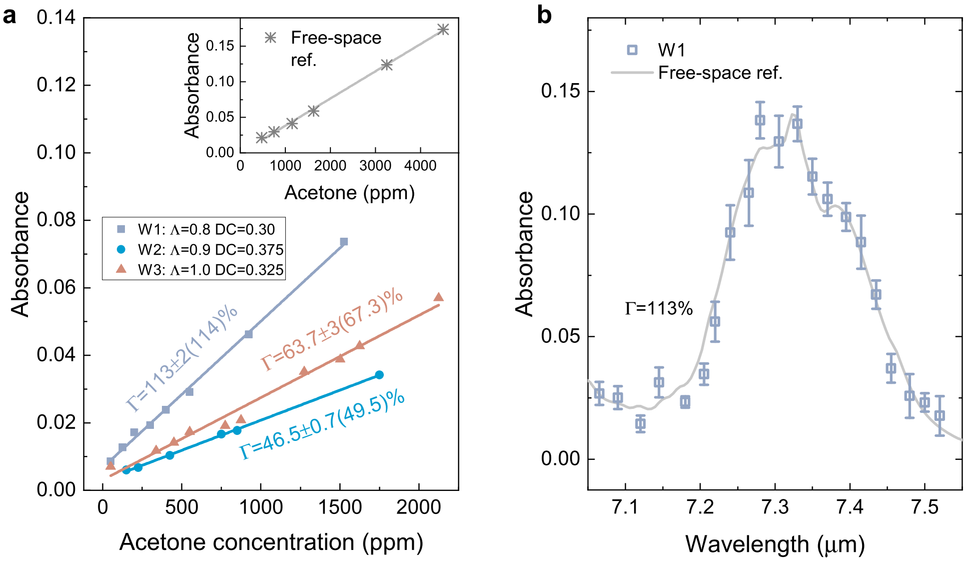

Figure 4. Validation of the external confinement factor of ADMAC waveguide. (a) Optical absorbances of three different ADMAC waveguides versus acetone concentrations, with identical propagation lengths of 10 mm. DC denotes the duty cycle. Inset: absorbance of the 10 mm path length free-space beam measured by FTIR. External confinement factors Γ of waveguides are calculated as the slope ratios of the fitted line of waveguides to that of a reference free-space beam. The values in parentheses are simulated values. (b) Absorption spectra of an ADMAC waveguide (Λ = 0.8 μm, DC = 0.3, averaged from three measurements) and free-space beam to 3250 ppm acetone. The free-space reference was scaled up by a Γ of 113%.

its Γ from 7.05 to 7.5 μm and measured the corresponding propagation loss (Figure 3d,e). As the wavelength increases from 7.05 to 7.5 μm, the Γ shows a slight increase from 109% to 117% while propagation loss maintains its low value below 6 dB/cm, confirming the subwavelength working status of the ADMAC waveguide. The propagation loss spectrum in Figure 3e shows an average of 5.1 dB/cm, and the representative cutback results at 7.33 μm give a propagation loss of 4.7 dB/cm (see Note 8 in the Supporting Information). Thanks to the less varied Γ and propagation loss, the ADMAC waveguide maintains a FOM above 0.85 cm over the entire measured wavelength range (Figure 3f). Various functional blocks are also demonstrated with excellent performance, including grating couplers for broad-band light coupling (3 dB bandwidth of 700 nm), mode converters for connection between strip waveguides and ADMAC waveguides (~0.11 dB transition loss), and 90° bends for waveguide curling (~0.12 dB/90° bending loss with a radius down to 50 μm) (see Notes 9 and 10 in the Supporting Information).

Acetone (C_3H_6O), a common building block in organic chemistry and an important breath marker for diabetes,[52,53] was selected as the analyte to examine the spectroscopic sensing performance of our waveguides. It processes a strong absorption peak in the LWIR region near 7.33 μm. During the characterization, acetone was diluted by nitrogen (N_2), and its concentration was precisely and dynamically controlled with a constant flow rate of 800 mL/min (see Note 5 in the Supporting Information for details). Figure 4a shows absorbance responses of three 10 mm long ADMAC waveguides (W1, W2, and W3) to different acetone concentrations ranging from 50 to 2250 ppm. Linear fits were employed to the recorded data, and sensitivities of 4.34×10^{-5}, 1.78×10^{-5}, and 2.44×10^{-5} per ppm were extracted for W1, W2, and W3, respectively. To validate the confinement factors of ADMAC waveguides, we compared their sensitivities to that of a 10 mm long free-space beam (Figure 4a, inset), which was acquired and fitted from Fourier-transform infrared spectroscopy (FTIR) measurements with the same gas generation setup and flow rate (see Note 5 in the Supporting Information for details). The Γ values were extracted as sensitivity ratios of ADMAC waveguides to the free-space reference. We find these confinement factor measurements give close matches to the simulated values. For the optimized waveguide W1, Γ is validated as 113 ± 2%. This corresponds to a free-space equivalent optical path length of 11.3 mm. Figure 4b shows the measured absorption spectra of waveguide W1 with 3250 ppm of acetone in the chamber, where the gray curve represents the free-space reference that was scaled up by 113%.

To further evaluate the minimum detectable acetone concentration and the stability of our sensor system, Allan deviation analysis was performed for continuous time-series measurements over 15 min with a sampling rate of 3 Hz.[54] The results are shown in Figure 5a, indicating that the system is dominated by white noise (with a slope of $\tau^{-1/2}$) for averaging times up to 20 s. For a sampling time of 0.33 s without any time-averaging process, the ADMAC waveguide achieves a 1 σ LoD of 10 ppm. At the optimum averaging time of 20 s, the LoD is evaluated to be 2.5 ppm, with a relative Allan deviation of 1×10^{-4}. For longer averaging times, the Allan deviation increases due to the drift of alignment stages (see Note 11 in the Supporting Information for a detailed noise analysis). Figure 5b shows two response-recovery cycles of the ADMAC waveguide to alternately injected 40 ppm acetone and pure N_2 without time averaging. The results are exponentially fitted and indicate a response time of ~3.8 s and a recovery time of ~6.6 s, which are limited by the gas exchanging time in the chamber.

We review and summarize the reported on-chip IR-TDLAS gas sensors and compare them with our work in Table 1. To the best of our knowledge, our ADMAC waveguide features a record high FOM, enabled by the extraordinary Γ and the comparable low propagation loss. It is worth noting that, in the SWIR region, TM-polarized waveguides are typically preferred over TE-polarized waveguides and claim better performance

https://doi.org/10.1021/acs.nanolett.2c01198
Nano Lett. 2022, 22, 6112−6120

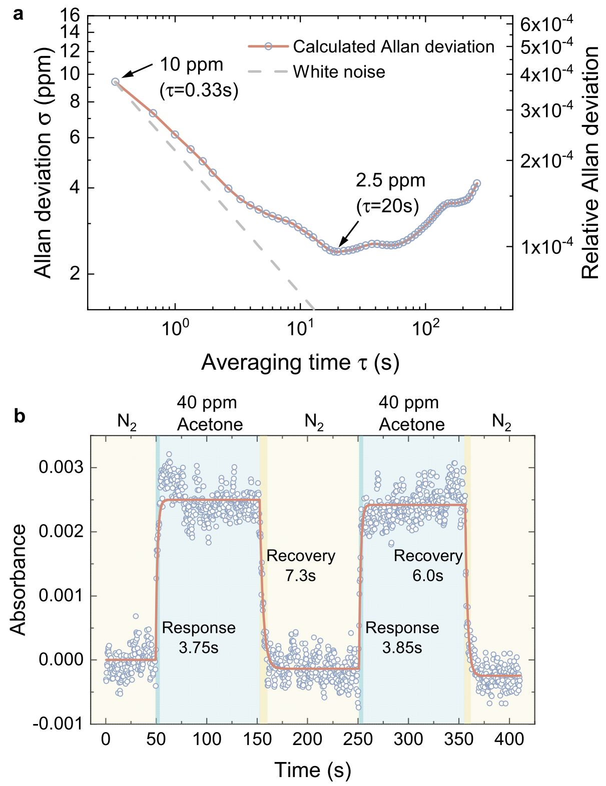

Figure 5. Allan deviation analysis and the dynamic response of the ADMAC waveguide. (a) Allan deviation as a function of the averaging time τ. The white noise with a slope of $\tau^{-1/2}$ is indicated by the dashed line. During the measurements, the gas chamber was constantly pumped with pure N_2. (b) Sensing response to alternating purged N_2 and 40 ppm acetone with a constant flow rate of 800 mL/min. The response time and recovery time are specified as the time required to reach 90% of the total signal change and are highlighted with dark green and dark yellow, respectively.

for absorption spectroscopy.[16,22] This is due to the relatively larger field penetrations into air claddings of TM-polarized waveguides as well as reduced scattering losses due to fewer overlaps between vertically distributed fields and rough etched sidewalls. Nevertheless, with the migration of operating wavelength from the SWIR to the MWIR and LWIR regions, the scattering loss is significantly suppressed, as it scales with λ^{-4}. This leads to more adoption of TE-polarized waveguides above 3 μm,[15,21,48,55] where TM-polarized waveguides may suffer from large substrate leakages due to the wide vertical field spread. Particularly, waveguides in an SWG metamaterial configuration are well-suited for MWIR/LWIR absorption spectroscopy, thanks to the suppressed sidewall-roughness scattering loss and reduced fabrication constraints in comparison with the SWIR region.[47] It is also worth noting that the presence of a bottom cladding layer in some of the reported works largely reduces the Γ and consequently decreases the sensitivity of gas detection.[15,55]

In comparison to bulk free-space TDLAS systems, the minimized waveguide sensors are inherently suitable for on-site applications and the deployment of distributed sensor nodes for the vigorously advanced Internet of things (IoT).[56−59] Examples include *in situ* monitoring for process control and exhaled breath analysis for medical diagnostics. For these cases, versatility and response speed are of equal importance to LoD. Therefore, alternative waveguide configurations to the conventional strip waveguide with larger Γ are preferred to boost the sensitivity, over the adoption of enrichment coatings with sacrificed versatility and response speed.[60−62] In our current ADMAC waveguide design, an LoD of 10 ppm to acetone has been demonstrated with a waveguide length of only 10 mm. In cases where an even lower LoD is desired, a longer waveguide length in excess of 100 mm can be potentially achieved within a small footprint, enabled by the low propagation and bending losses. Therefore, it is expected that we could push the minimum detectable concentration of most gases down to sub-ppm levels without any enrichment coating, while the corresponding response time, which can be rationally believed, is still within 5 s.

In conclusion, we have demonstrated a Si ADMAC waveguide for sensitive and fast LWIR gas spectroscopy. By leveraging the large longitudinal electric field discontinuity at periodic high-index-contrast interfaces in the SWG metamaterial and its unique features in RI engineering, we achieve an Γ of 113% in the ADMAC waveguide with a low propagation loss. Consequently, a record high FOM of 1.03 cm is demonstrated. Thanks to this, the spectroscopic sensing of acetone on a 10 mm long waveguide achieves a 10 ppm LoD with a fast dynamic response, which can be further decreased to 2.5 ppm with a moderate averaging time or even sub-ppm with an increased waveguide length. Built on the most mature SOI platform with single-step lithography, our ADMAC waveguide sensor is ready to take advantage of cost-effective CMOS fabrication techniques and abundant infrastructure to enable mass production and large-scale on-site deployment for widespread IoT sensing applications.

■ ASSOCIATED CONTENT

Supporting Information

The Supporting Information is available free of charge at https://pubs.acs.org/doi/10.1021/acs.nanolett.2c01198.

Table 1. Comparison of On-Chip IR-TDLAS Gas Sensors

platform	λ (μm)	Γ (%)	loss (dB/cm)	FOM (cm)	waveguide length (mm)	LoD (ppm)	AT/RT (s)[c]	ref
SOI[a]	7.33	113	4.7 (TE)	1.03	10	10 (acetone)	3.8 (RT)	this work
						2.5 (acetone)	20 (AT)	this work
SOI[a]	6.65	24.3	3.9 (TE)	0.3	28.4	25 (toluene)	0.8 (RT)	48
SON[b]	4.26	14	4.0 (TE)	0.15	20	500 (CO_2)	60 (RT)	55
SOI[a]	4.24	44	3 (TE)	0.63	—	100 (CO_2)	2 (RT)	21
SOI	3.9	14	4 (TE)	0.15	7.5	600 (N_2O)	6 (RT)	15
Ta_2O_5[a]	2.57	107	6.8 (TM)	0.69	20	7 (C_2H_2)	25 (AT)	22
SOI	1.65	25.4	2 (TM)	0.55	100	100 (CH_4)	60 (AT)	16

[a]With a free-standing configuration. [b]SON: silicon-on-silicon nitride. [c]Abbreviations: AT, averaging time; RT, response time.

Equivalent RI of SWG metamaterials, electric field in ADMAC waveguide, simulation of ADMAC waveguide, FOM for on-chip IR-TDLAS sensors, waveguide characterizations and spectroscopic measurements, waveguide fabrication, summary of MWIR/LWIR waveguide platforms, waveguide cutback measurements, functional blocks of ADMAC waveguides, summary of MWIR/LWIR grating couplers, an noise analysis (PDF)

AUTHOR INFORMATION

Corresponding Author

Chengkuo Lee − *Department of Electrical and Computer Engineering, National University of Singapore, Singapore 117583, Singapore; Center for Intelligent Sensors and MEMS (CISM), National University of Singapore, Singapore 117608, Singapore;* orcid.org/0000-0002-8886-3649; Email: elelc@nus.edu.sg

Authors

Weixin Liu − *Department of Electrical and Computer Engineering, National University of Singapore, Singapore 117583, Singapore; Center for Intelligent Sensors and MEMS (CISM), National University of Singapore, Singapore 117608, Singapore;* orcid.org/0000-0002-5526-3487

Yiming Ma − *Department of Electrical and Computer Engineering, National University of Singapore, Singapore 117583, Singapore; Center for Intelligent Sensors and MEMS (CISM), National University of Singapore, Singapore 117608, Singapore;* orcid.org/0000-0002-5730-3956

Xinmiao Liu − *Department of Electrical and Computer Engineering, National University of Singapore, Singapore 117583, Singapore; Center for Intelligent Sensors and MEMS (CISM), National University of Singapore, Singapore 117608, Singapore*

Jingkai Zhou − *Department of Electrical and Computer Engineering, National University of Singapore, Singapore 117583, Singapore; Center for Intelligent Sensors and MEMS (CISM), National University of Singapore, Singapore 117608, Singapore*

Cheng Xu − *Department of Electrical and Computer Engineering, National University of Singapore, Singapore 117583, Singapore; Center for Intelligent Sensors and MEMS (CISM), National University of Singapore, Singapore 117608, Singapore*

Bowei Dong − *Department of Electrical and Computer Engineering, National University of Singapore, Singapore 117583, Singapore; Center for Intelligent Sensors and MEMS (CISM), National University of Singapore, Singapore 117608, Singapore*

Complete contact information is available at: https://pubs.acs.org/10.1021/acs.nanolett.2c01198

Author Contributions

[§]W.L. and Y.M. contributed equally.

Notes

The authors declare no competing financial interest.

ACKNOWLEDGMENTS

This research was supported by the National Research Foundation Competitive Research Programme (NRF-CRP15-2015-02), Ministry of Education (MOE) Singapore Tier two project (MOE-T2EP50220-0014; A-0009520-01-00), and the Advanced Research and Technology Innovation Centre (A-0005947-20-00) at NUS, Singapore.

REFERENCES

(1) Altug, H.; Oh, S. H.; Maier, S. A.; Homola, J. Advances and Applications of Nanophotonic Biosensors. *Nat. Nanotechnol.* **2022**, *17* (1), 5−16.

(2) Reese, T.; Reed, A. N.; Sample, A. D.; Freire-Fernández, F.; Schaller, R. D.; Urbas, A. M.; Odom, T. W. Ultrafast Spectroscopy of Plasmonic Titanium Nitride Nanoparticle Lattices. *ACS Photonics* **2021**, *8* (6), 1556−1561.

(3) Zhou, H.; Hui, X.; Li, D.; Hu, D.; Chen, X.; He, X.; Gao, L.; Huang, H.; Lee, C.; Mu, X. Metal−Organic Framework-Surface-Enhanced Infrared Absorption Platform Enables Simultaneous On-Chip Sensing of Greenhouse Gases. *Adv. Sci.* **2020**, *7* (20), 2001173.

(4) Wei, J.; Xu, C.; Dong, B.; Qiu, C.-W. W.; Lee, C. Mid-Infrared Semimetal Polarization Detectors with Configurable Polarity Transition. *Nat. Photonics* **2021**, *15* (8), 614−621.

(5) Solomon, M. L.; Hu, J.; Lawrence, M.; García-Etxarri, A.; Dionne, J. A. Enantiospecific Optical Enhancement of Chiral Sensing and Separation with Dielectric Metasurfaces. *ACS Photonics* **2019**, *6* (1), 43−49.

(6) Tittl, A.; Leitis, A.; Liu, M.; Yesilkoy, F.; Choi, D.-Y.; Neshev, D. N.; Kivshar, Y. S.; Altug, H. Imaging-Based Molecular Barcoding with Pixelated Dielectric Metasurfaces. *Science (80-.)* **2018**, *360* (6393), 1105−1109.

(7) Xu, X.; Xu, R.; Lin, Y.-S. A Voltage-Controllable VO_2 Based Metamaterial Perfect Absorber for CO_2 Gas Sensing Application. *Nanoscale* **2022**, *14* (7), 2722−2728.

(8) Zhan, F.; Lin, Y.-S. Tunable Multiresonance Using Complementary Circular Metamaterial. *Opt. Lett.* **2020**, *45* (13), 3633−3636.

(9) Zhang, Y.; Lin, P.; Lin, Y.-S. Tunable Split-Disk Metamaterial Absorber for Sensing Application. *Nanomaterials* **2021**, *11* (3), 598.

(10) Dong, L.; Tittel, F. K.; Li, C.; Sanchez, N. P.; Wu, H.; Zheng, C.; Yu, Y.; Sampaolo, A.; Griffin, R. J. Compact TDLAS Based Sensor Design Using Interband Cascade Lasers for Mid-IR Trace Gas Sensing. *Opt. Express* **2016**, *24* (6), A528−A535.

(11) Ma, Y.; Chang, Y.; Dong, B.; Wei, J.; Liu, W.; Lee, C. Heterogeneously Integrated Graphene/Silicon/Halide Waveguide Photodetectors toward Chip-Scale Zero-Bias Long-Wave Infrared Spectroscopic Sensing. *ACS Nano* **2021**, *15* (6), 10084−10094.

(12) Han, Z.; Lin, P.; Singh, V.; Kimerling, L.; Hu, J.; Richardson, K.; Agarwal, A.; Tan, D. T. H. H. On-Chip Mid-Infrared Gas Detection Using Chalcogenide Glass Waveguide. *Appl. Phys. Lett.* **2016**, *108* (14), 141106.

(13) Hu, T.; Dong, B.; Luo, X.; Liow, T.-Y.; Song, J.; Lee, C.; Lo, G.-Q. Silicon Photonic Platforms for Mid-Infrared Applications. *Photonics Res.* **2017**, *5* (5), 417−430.

(14) Chen, C.; Mohr, D. A.; Choi, H. K.; Yoo, D.; Li, M.; Oh, S. H. Waveguide-Integrated Compact Plasmonic Resonators for On-Chip Mid-Infrared Laser Spectroscopy. *Nano Lett.* **2018**, *18* (12), 7601−7608.

(15) Yazici, M. S.; Dong, B.; Hasan, D.; Sun, F.; Lee, C. Integration of MEMS IR Detectors with MIR Waveguides for Sensing Applications. *Opt. Express* **2020**, *28* (8), 11524−11537.

(16) Tombez, L.; Zhang, E. J.; Orcutt, J. S.; Kamlapurkar, S.; Green, W. M. J. Methane Absorption Spectroscopy on a Silicon Photonic Chip. *Optica* **2017**, *4* (11), 1322.

(17) Chen, Y.; Lin, H.; Hu, J.; Li, M. Heterogeneously Integrated Silicon Photonics for the Mid-Infrared and Spectroscopic Sensing. *ACS Nano* **2014**, *8* (7), 6955−6961.

(18) Ma, Y.; Dong, B.; Lee, C. Progress of Infrared Guided-Wave Nanophotonic Sensors and Devices. *Nano Converg.* **2020**, *7* (1), 12.

(19) Lin, H.; Luo, Z.; Gu, T.; Kimerling, L. C.; Wada, K.; Agarwal, A.; Hu, J. Mid-Infrared Integrated Photonics on Silicon: A Perspective. *Nanophotonics* **2017**, *7* (2), 393−420.

(20) Robinson, J. T.; Preston, K.; Painter, O.; Lipson, M. First-Principle Derivation of Gain in High-Index-Contrast Waveguides. *Opt. Express* **2008**, *16* (21), 16659.

(21) Ottonello-Briano, F.; Errando-Herranz, C.; Rödjegård, H.; Martin, H.; Sohlström, H.; Gylfason, K. B. Carbon Dioxide Absorption Spectroscopy with a Mid-Infrared Silicon Photonic Waveguide. *Opt. Lett.* **2020**, *45* (1), 109−112.
(22) Vlk, M.; Datta, A.; Alberti, S.; Yallew, H. D.; Mittal, V.; Factor, S. C.; Murugan, G. S.; Jágerská, J.; Factor, S. C. Extraordinary Evanescent Field Confinement Waveguide Sensor for Mid-Infrared Trace Gas Spectroscopy. *Light Sci. Appl.* **2021**, *10* (1), 26.
(23) Zou, Y.; Chakravarty, S.; Wray, P.; Chen, R. T. Mid-Infrared Holey and Slotted Photonic Crystal Waveguides in Silicon-on-Sapphire for Chemical Warfare Simulant Detection. *Sensors Actuators, B Chem.* **2015**, *221*, 1094−1103.
(24) Goyal, A. K.; Dutta, H. S.; Pal, S. Recent Advances and Progress in Photonic Crystal-Based Gas Sensors. *J. Phys. D. Appl. Phys.* **2017**, *50* (20), 203001.
(25) Jahani, S.; Jacob, Z. All-Dielectric Metamaterials. *Nat. Nanotechnol.* **2016**, *11* (1), 23−36.
(26) Xu, R.; Lin, Y.-S. Flexible and Controllable Metadevice Using Self-Assembly MEMS Actuator. *Nano Lett.* **2021**, *21* (7), 3205−3210.
(27) Klopfer, E.; Dagli, S.; Barton, D.; Lawrence, M.; Dionne, J. A. High-Quality-Factor Silicon-on-Lithium Niobate Metasurfaces for Electro-Optically Reconfigurable Wavefront Shaping. *Nano Lett.* **2022**, *22* (4), 1703−1709.
(28) Lawrence, M.; Barton, D. R.; Dionne, J. A. Nonreciprocal Flat Optics with Silicon Metasurfaces. *Nano Lett.* **2018**, *18* (2), 1104−1109.
(29) Ao, X.; Wang, D.; Odom, T. W. Enhanced Fields in Mirror-Backed Low-Index Dielectric Structures. *ACS Photonics* **2019**, *6* (11), 2612−2617.
(30) Xu, R.; Xu, X.; Yang, B.-R.; Gui, X.; Qin, Z.; Lin, Y.-S. Actively Logical Modulation of MEMS-Based Terahertz Metamaterial. *Photonics Res.* **2021**, *9* (7), 1409−1415.
(31) Wang, Z.; Li, T.; Soman, A.; Mao, D.; Kananen, T.; Gu, T. On-Chip Wavefront Shaping with Dielectric Metasurface. *Nat. Commun.* **2019**, *10* (1), 3547.
(32) Ren, Z.; Dong, B.; Qiao, Q.; Liu, X.; Liu, J.; Zhou, G.; Lee, C. Subwavelength On-chip Light Focusing with Bigradient All-dielectric Metamaterials for Dense Photonic Integration. *InfoMat* **2022**, *4* (2), e12264.
(33) Shen, B.; Wang, P.; Polson, R.; Menon, R. An Integrated-Nanophotonics Polarization Beamsplitter with 2.4 × 2.4 μm^2 Footprint. *Nat. Photonics* **2015**, *9* (6), 378−382.
(34) Halir, R.; Cheben, P.; Luque-González, J. M.; Sarmiento-Merenguel, J. D.; Schmid, J. H.; Wangüemert-Pérez, G.; Xu, D. X.; Wang, S.; Ortega-Moñux, A.; Molina-Fernández, Í. Ultra-Broadband Nanophotonic Beamsplitter Using an Anisotropic Sub-Wavelength Metamaterial. *Laser Photonics Rev.* **2016**, *10* (6), 1039−1046.
(35) Jahani, S.; Kim, S.; Atkinson, J.; Wirth, J. C.; Kalhor, F.; Noman, A. Al; Newman, W. D.; Shekhar, P.; Han, K.; Van, V.; DeCorby, R. G.; Chrostowski, L.; Qi, M.; Jacob, Z. Controlling Evanescent Waves Using Silicon Photonic All-Dielectric Metamaterials for Dense Integration. *Nat. Commun.* **2018**, *9* (1), 1893.
(36) Mia, M. B.; Ahmed, S. Z.; Ahmed, I.; Lee, Y. J.; Qi, M.; Kim, S. Exceptional Coupling in Photonic Anisotropic Metamaterials for Extremely Low Waveguide Crosstalk. *Optica* **2020**, *7* (8), 881.
(37) Staude, I.; Schilling, J. Metamaterial-Inspired Silicon Nanophotonics. *Nat. Photonics* **2017**, *11* (5), 274−284.
(38) Zou, Y.; Chakravarty, S.; Chung, C.-J.; Xu, X.; Chen, R. T. Mid-Infrared Silicon Photonic Waveguides and Devices. *Photonics Res.* **2018**, *6* (4), 254.
(39) Lin, P. T.; Kwok, S. W.; Lin, H. Y. G.; Singh, V.; Kimerling, L. C.; Whitesides, G. M.; Agarwal, A. Mid-Infrared Spectrometer Using Opto-Nanofluidic Slot-Waveguide for Label-Free on-Chip Chemical Sensing. *Nano Lett.* **2014**, *14* (1), 231−238.
(40) Soref, R. A.; Emelett, S. J.; Buchwald, W. R. Silicon Waveguided Components for the Long-Wave Infrared Region. *J. Opt. A Pure Appl. Opt.* **2006**, *8* (10), 840−848.
(41) Dong, B.; Guo, X.; Ho, C. P.; Li, B.; Wang, H.; Lee, C.; Luo, X.; Lo, G.-Q. Silicon-on-Insulator Waveguide Devices for Broadband Mid-Infrared Photonics. *IEEE Photonics J.* **2017**, *9* (3), 1.
(42) Lee, C.; Radhakrishnan, R.; Chen, C.-C.; Li, J.; Thillaigovindan, J.; Balasubramanian, N. Design and Modeling of a Nanomechanical Sensor Using Silicon Photonic Crystals. *J. Light. Technol.* **2008**, *26* (7), 839−846.
(43) Lin, Y. S.; Xu, Z. Reconfigurable Metamaterials for Optoelectronic Applications. *Int. J. Optomechatronics* **2020**, *14* (1), 78−93.
(44) Cheben, P.; Halir, R.; Schmid, J. H.; Atwater, H. A.; Smith, D. R. Subwavelength Integrated Photonics. *Nature* **2018**, *560* (7720), 565−572.
(45) Qiao, Q.; Sun, H.; Liu, X.; Dong, B.; Xia, J.; Lee, C.; Zhou, G. Suspended Silicon Waveguide with Sub-Wavelength Grating Cladding for Optical MEMS in Mid-Infrared. *Micromachines* **2021**, *12* (11), 1311.
(46) Driscoll, J. B.; Liu, X.; Yasseri, S.; Hsieh, I.; Dadap, J. I.; Osgood, R. M. Large Longitudinal Electric Fields (E_z) in Silicon Nanowire Waveguides. *Opt. Express* **2009**, *17* (4), 2797−2804.
(47) Kita, D. M.; Michon, J.; Johnson, S. G.; Hu, J. Are Slot and Sub-Wavelength Grating Waveguides Better than Strip Waveguides for Sensing? *Optica* **2018**, *5* (9), 1046−1054.
(48) Liu, W.; Ma, Y.; Chang, Y.; Dong, B.; Wei, J.; Ren, Z.; Lee, C. Suspended Silicon Waveguide Platform with Subwavelength Grating Metamaterial Cladding for Long-Wave Infrared Sensing Applications. *Nanophotonics* **2021**, *10* (7), 1861−1870.
(49) Penadés, J. S.; Sánchez-Postigo, A.; Nedeljkovic, M.; Ortega-Moñux, A.; Wangüemert-Pérez, J. G.; Xu, Y.; Halir, R.; Qu, Z.; Khokhar, A. Z.; Osman, A.; Cao, W.; Littlejohns, C. G.; Cheben, P.; Molina-Fernández, I.; Mashanovich, G. Z. Suspended Silicon Waveguides for Long-Wave Infrared Wavelengths. *Opt. Lett.* **2018**, *43* (4), 795−798.
(50) Nedeljkovic, M.; Penades, J. S.; Mittal, V.; Murugan, G. S.; Khokhar, A. Z.; Littlejohns, C.; Carpenter, L. G.; Gawith, C. B. E.; Wilkinson, J. S.; Mashanovich, G. Z. Germanium-on-Silicon Waveguides Operating at Mid-Infrared Wavelengths up to 8.5 μm. *Opt. Express* **2017**, *25* (22), 27431−27441.
(51) Ramirez, J. M.; Liu, Q.; Vakarin, V.; Frigerio, J.; Ballabio, A.; Le Roux, X.; Bouville, D.; Vivien, L.; Isella, G.; Marris-Morini, D. Graded SiGe Waveguides with Broadband Low-Loss Propagation in the Mid Infrared. *Opt. Express* **2018**, *26* (2), 870−877.
(52) Righettoni, M.; Tricoli, A. Toward Portable Breath Acetone Analysis for Diabetes Detection. *J. Breath Res.* **2011**, *5* (3), 037109.
(53) Zhu, J.; Ren, Z.; Lee, C. Toward Healthcare Diagnoses by Machine-Learning-Enabled Volatile Organic Compound Identification. *ACS Nano* **2021**, *15* (1), 894−903.
(54) Werle, P.; Mücke, R.; Slemr, F. The Limits of Signal Averaging in Atmospheric Trace-Gas Monitoring by Tunable Diode-Laser Absorption Spectroscopy (TDLAS). *Appl. Phys. B Photophysics Laser Chem.* **1993**, *57* (2), 131−139.
(55) Ranacher, C.; Consani, C.; Vollert, N.; Tortschanoff, A.; Bergmeister, M.; Grille, T.; Jakoby, B. Characterization of Evanescent Field Gas Sensor Structures Based on Silicon Photonics. *IEEE Photonics J.* **2018**, *10* (5), 1−14.
(56) Hodgkinson, J.; Tatam, R. P. Optical Gas Sensing: A Review. *Meas. Sci. Technol.* **2013**, *24* (1), 012004.
(57) Huang, L.; Dong, B.; Guo, X.; Chang, Y.; Chen, N.; Huang, X.; Liao, W.; Zhu, C.; Wang, H.; Lee, C.; Ang, K.-W. W. Waveguide-Integrated Black Phosphorus Photodetector for Mid-Infrared Applications. *ACS Nano* **2019**, *13* (1), 913−921.
(58) Youngblood, N.; Chen, C.; Koester, S. J.; Li, M. Waveguide-Integrated Black Phosphorus Photodetector with High Responsivity and Low Dark Current. *Nat. Photonics* **2015**, *9* (4), 247−252.
(59) Liu, X.; Liu, W.; Ren, Z.; Ma, Y.; Dong, B.; Zhou, G.; Lee, C. Progress of Optomechanical Micro/Nano Sensors : A Review. *Int. J. Optomechatronics* **2021**, *15* (1), 120−159.
(60) Tuerdi, G.; Kari, N.; Yan, Y.; Nizamidin, P.; Yimit, A. A Functionalized Tetrakis(4-Nitrophenyl)Porphyrin Film Optical

Waveguide Sensor for Detection of H_2S and Ethanediamine Gases. *Sensors* **2017**, *17* (12), 2717.
(61) Ablat, H.; Yimit, A.; Mahmut, M.; Itoh, K. Nafion Film/K^+-Exchanged Glass Optical Waveguide Sensor for BTX Detection. *Anal. Chem.* **2008**, *80* (20), 7678−7683.
(62) Mironenko, A. Y.; Sergeev, A. A.; Nazirov, A. E.; Modin, E. B.; Voznesenskiy, S. S.; Bratskaya, S. Y. H_2S Optical Waveguide Gas Sensors Based on Chitosan/Au and Chitosan/Ag Nanocomposites. *Sensors Actuators B Chem.* **2016**, *225*, 348−353.